Extended finite element modeling of deformable porous media with arbitrary interfaces

A.R. Khoei *, E. Haghighat

Center of Excellence in Structures and Earthquake Engineering, Department of Civil Engineering, Sharif University of Technology, P.O. Box 11365-9313, Tehran, Iran

ABSTRACT

In this paper, an enriched finite element method is presented for numerical simulation of saturated porous media. The arbitrary discontinuities, such as material interfaces, are encountered via the extended finite element method (X-FEM) by enhancing the standard FEM displacements. The X-FEM technique is applied to the governing equations of porous media for the spatial discretization, followed by a generalized Newmark scheme used for the time domain discretization. In X-FEM, the material interfaces are represented independently of element boundaries and the process is accomplished by partitioning the domain with some triangular sub-elements whose Gauss points are used for integration of the domain of elements. Finally, several numerical examples are analyzed, including the dynamic analysis of the failure of lower San Fernando dam, to demonstrate the efficiency of the X-FEM technique in saturated porous soils.

1. Introduction

Porous media is a composition of the solid phase which is referred as solid skeleton and closed and open pores which may fill with a pore fluid. The solid and fluid phases usually have a relative velocity with each other, and they also have different material properties. Thus, there is an interaction between these phases. Except some special loading conditions, the complete prediction of behavior of the solid material deformation interacting with a fluid flow is achieved by a complete solution of porous media coupled governing equations which is described in following sections. This interaction is much important in dynamic loading with low permeability values, such as earthquake loading of dams and other engineering soil structures. Basically, different kinematical and mechanical variables are considered for each phase of porous media, in which the strain and stress components are decomposed for each phase. The stress acting between solid grains is referred as effective stress while the decomposed hydrostatic stress acting on fluid phases are referred as excess pore pressure.

The flow problem in deforming porous media has been a topic of interest to research workers for a considerable time. A complete review of the history of development of porous media theories is given by de Boer [1]. In order to present an introductory review of developed theories, the Terzaghi theory can be referred as the first study in deformable porous media which was lead to the one dimensional consolidation theory on the basis of effective stress concept [2]. This theory was extended to three dimensional cases by Biot [3–5]. Modern mixture theories were developed based on the concept of volume fractions by Morland [6], Goodman and Cowin [7], Sampaio and Williams [8] and Bowen [9,10]. Averaging theories were developed by Whitaker [11] and Hassanizadeh and Gary [12–14]. The Biot theory was extended to three-phase conditions with a pore air as the third phase by Fredlund and Morgenstern [15] and Chang and Duncan [16]. The theory was developed by de Boer and Kowalski [17] on material non-linearity behavior of the soil skeleton in the Terzaghi–Biot framework. A

---

* Corresponding author. Tel.: +98 (21) 6600 5818; fax: +98 (21) 6601 4828.
  E-mail address: arkhoei@sharif.edu (A.R. Khoei).

generalized incremental form which includes large deformation and nonlinear material behavior was derived by Zienkiewicz et al. [18] for liquefaction analysis of soil structures. A simple extension on two-phase formulation of porous media considering the air pressure to be constant and equal to the atmospheric pressure was proposed by Zienkiewicz et al. [19]. Coupled formulations that involve the air and water phases in soils were proposed by Alonso et al. [20], Schrefler and Zhan [21] and Gawin et al. [22,23]. The aim of this study is to model the deformable porous media with arbitrary interfaces using an enriched finite element model based on the X-FEM technique.

The eXtended Finite Element Method (X-FEM) is a powerful and accurate approach to model discontinuities, which are independent of the FE mesh topology. The technique has been successfully applied to problems exhibiting discontinuities and inhomogeneities, such as cracks, holes, or material interfaces. In this method, the discontinuities, or interfaces, are not considered in the mesh generation operation and special functions, which depend on the nature of discontinuity, are included into the finite element approximation through a partition of unity method [24]. The technique was first introduced by Dolbow [25], Belytschko and Black [26] and Moës et al. [27] to model cracks and inhomogeneities. The method allows modeling the entire crack geometry independently of the mesh, and completely avoids the need to regenerate the mesh as the crack grows. The X-FEM was used to model the crack growth and arbitrary discontinuities by enriching the discontinuous approximation in terms of a signed distance and level sets functions [28–30]. The technique was applied in linear crack problems, including: the crack growth with frictional contact [31], cohesive crack propagation [32], stationary and growing cracks [33], three-dimensional crack propagation [34], and fluid flow in fractured deforming porous media [35]. An overview of the technique was addressed by Bordas et al. [36] in the framework of an object-oriented-enriched finite element programming. The X-FEM was employed in elasto-plasticity problems, including: the crack propagation in plastic fracture mechanics [37,38], the plasticity of frictional contact on arbitrary interfaces [39,40], the large X-FEM deformation [41,42], the ALE-XFEM model for large plastic deformation [43,44], the localization phenomenon in higher-order Cosserat theory [45].

In the present paper, the extended finite element method is applied to the governing equations of porous media in an updated Lagrangian framework, followed by a generalized Newmark scheme used for the time domain discretization. The X-FEM is used in modeling weak discontinuities, in which the process is accomplished by partitioning the domain with some triangular sub-elements whose Gauss points are used for the integration of the domain of elements. The internal interfaces are modeled by additional degrees-of-freedom, known as the enriched DOFs. Numerical examples of saturated porous soils are modeled to illustrate the capability of proposed computational algorithm and the results are compared with those of standard FEM model.

2. Governing equations of deformable porous media

Porous material is a composition of solid grains, or skeleton, and pore, which fills with at least one or more fluids. In most applications, pores are filled partially with water and partially with moist air. The degree of saturation of each fluid phase in a representative elementary volume (REV) is defined as the ratio of its pore space to the total void space. Thus, the water and gas saturation ratios are respectively defined as

$$S_w = \frac{dV_w}{dV_w + dV_g}, \quad S_g = \frac{dV_g}{dV_w + dV_g}, \tag{1}$$

where w and g refers to the water and gas phases, respectively, S is the phase saturation, and dV is referred as the volume fraction. It is obvious that for two-phase fluid flow $S_w + S_g = 1$. The porosity is defined as the ratio of pore space to the total volume, i.e. $n = dV_v/dV_s$, with dV_v denoting the sum of phase pore spaces. Neglecting the mass density of gas phase, the density can be computed for the total soil-fluid mixture as

$$\rho = n\rho_v + (1 - n)\rho_s \approx n\rho_w + (1 - n)\rho_s. \tag{2}$$

The stress at each point is decomposed into the effective stress which acts between the solid grains and controls their loading capacity and deformation, and the average pore pressure of fluid phases which participates in load bearing of the total soil sample. Thus, the total stress tensor $\boldsymbol{\sigma}$ can be defined as $\boldsymbol{\sigma} = \boldsymbol{\sigma}' - \alpha p \, \mathbf{I}$, with $\boldsymbol{\sigma}'$ denoting the effective stress and α a corrective coefficient of pore pressure effect on solid grains, in which for isotropic materials defined by $\alpha = 1 - K_T/K_S$, where K_T and K_S are the bulk modulus of soil sample and solid grains, respectively, and for most soils $\alpha \approx 1$. The average pore pressure of fluid phase p is defined as

$$p = \chi_w p_w + \chi_g p_g, \tag{3}$$

where χ_w and χ_g are coefficients which depend on the water and gas interfaces with solid grains and can be approximated by S_w and S_g.

In order to derive the governing equations of porous media, the Biot theory is employed in an updated Lagrangian framework. Consider a two-phase media, in which the fluid phase is partially saturated under the condition of $p_g = 0$, and the convective terms are neglected. The motion of total mixture is defined by the motion of solid–fluid mixture $u_i(\mathbf{x}, t)$ and the relative motion of fluid with respect to the mixture $w_i(\mathbf{x}, t)$. The governing equations are the total solid–fluid mixture, the

linear momentum-balance and the continuity equation for each phase. The linear momentum-balance of solid–fluid mixture can be written as

$$\mathrm{div}\,\boldsymbol{\sigma} - \rho\ddot{\mathbf{u}} + \rho\mathbf{b} = 0. \tag{4}$$

The momentum-balance of the fluid phase leads to

$$-\nabla p - \mathbf{R} - \rho_f\ddot{\mathbf{u}} + \rho_f\mathbf{b} = 0, \tag{5}$$

where $\mathbf{R}$ represents the viscous drag force defined by the Darcy seepage law as $\mathbf{kR = w}$, with $\mathbf{k}$ denoting the permeability matrix with the dimension of (length)^3(time)/(mass). Finally, the continuity equation of fluid phase can be written as

$$\mathrm{div}\,\mathbf{w} + \alpha\mathrm{tr}\,\dot{\boldsymbol{\varepsilon}} + \left(\frac{n}{K_f} + \frac{\alpha - n}{K_s}\right)\dot{p} + \dot{S} = 0. \tag{6}$$

Eqs. (4)–(6) are the coupled governing equations of porous saturated media with variable-set (u_i, w_i, p). Performing some mathematical manipulations, the set of equations can be modified as $u - p$ formulation of porous media which is appropriate to model the partially saturated porous material subjected to earthquake loading frequencies. Combining Eqs. (5) and (6) results in

$$\mathrm{div}\left[\mathbf{k}(-\nabla p - S_w\rho_f\ddot{\mathbf{u}} + S_w\rho_f\mathbf{b})\right] + \alpha\mathrm{tr}\,\dot{\boldsymbol{\varepsilon}} + \frac{1}{Q^*}\dot{p} + \dot{S} = 0, \tag{7}$$

where

$$\frac{1}{Q^*} \equiv C_s + \frac{nS_w}{K_f} + \frac{(\alpha - n)\chi_w}{K_s}, \quad n\frac{dS_w(p_w)}{dt} = n\frac{dS_w(p_w)}{dp_w}\frac{dp_w}{dt} = C_s\dot{p}_w, \tag{8}$$

where $C_s = ndS_w/dp_w$. For fully saturated conditions $C_s = 0$, however, in unsaturated conditions, it is proportional to the slope of $S_w - P_w$ curve. Eqs. (4) and (7) are complemented by appropriate kinematical relation and the stress–strain constitutive equation [46]. The kinematic equation is defined by the incremental strain–displacement relationship, and the stress–strain constitutive equation is defined by $d\boldsymbol{\sigma}' = \mathbf{D}d\boldsymbol{\varepsilon}$, with $\mathbf{D}$ denoting the forth order tangential stiffness matrix computed using an appropriate constitutive law.

The introduced governing equations form the boundary value problem, which can be solved using the appropriate initial and boundary conditions. The solid-phase boundary conditions are $\mathbf{u} = \bar{\mathbf{u}}$ on $\Gamma = \Gamma_u$ and $\mathbf{t} = \boldsymbol{\sigma}\mathbf{n} \equiv \bar{\mathbf{t}}$ on $\Gamma = \Gamma_t$, in which $\Gamma = \Gamma_t \cup \Gamma_u$ is the boundary of domain. The fluid-phase boundary conditions are $\mathbf{p} = \bar{\mathbf{p}}$ on $\Gamma = \Gamma_p$ and $\mathbf{n}.\mathbf{w} = \mathbf{n} \cdot \mathbf{k}(-\nabla p_w + S_w\rho_f\mathbf{b}) = \widehat{\mathbf{w}}_n$ on $\Gamma = \Gamma_w$ with $\Gamma = \Gamma_p \cup \Gamma_w$.

3. Extended FEM formulation of deformable porous equations

In order to derive the weak form of governing Eqs. (4) and (7), the trial functions $\mathbf{u}(\mathbf{x}, t)$ and $p_w(\mathbf{x}, t)$ are required to satisfy all essential boundary conditions and to be smooth enough to define the derivatives of equations. In addition, the test functions $\delta\mathbf{u}(\mathbf{x}, t)$ and $\delta p_w(\mathbf{x}, t)$ are required to be smooth enough to be vanished on the prescribed strong boundary conditions. To obtain the weak form of governing equations, the test functions $\delta\mathbf{u}(\mathbf{x}, t)$ and $\delta p_w(\mathbf{x}, t)$ are respectively multiplied by Eqs. (4) and (7) and integrated over the domain Ω as

$$\int_\Omega \delta\mathbf{u}(\nabla\boldsymbol{\sigma} - \rho\ddot{\mathbf{u}} + \rho\mathbf{b})d\Omega = 0,$$
$$\int_\Omega \delta p_w\left(\mathrm{div}\left[\mathbf{k}(-\nabla p - S_w\rho_f\ddot{\mathbf{u}} + S_w\rho_f\mathbf{b})\right] + \alpha\mathrm{tr}\,\dot{\boldsymbol{\varepsilon}} + \frac{1}{Q^*}\dot{p} + \dot{S}\right)d\Omega = 0. \tag{9}$$

Expanding the above integral equations and using the Divergence theorem leads to the following weak form of governing equations as

$$\int_\Omega \delta\mathbf{u}\rho\ddot{\mathbf{u}}d\Omega + \int_\Omega \nabla\delta\mathbf{u} : \sigma d\Omega = \int_\Omega \delta\mathbf{u}\rho\mathbf{b}d\Omega + \int_\Gamma \delta\mathbf{u}\bar{\mathbf{t}}d\Gamma,$$
$$\int_\Omega \delta p_w\alpha\mathrm{tr}\,\dot{\boldsymbol{\varepsilon}}d\Omega + \int_\Omega \nabla\delta p_w\mathbf{k}\nabla p_w d\Omega + \int_\Omega \delta p_w\frac{1}{Q^*}\dot{p}_w d\Omega$$
$$= \int_\Gamma \delta p_w(\mathbf{nk}\nabla p_w)d\Gamma - \int_\Omega \nabla\delta p_w\mathbf{k}(S_w\rho_f\mathbf{b})d\Omega. \tag{10}$$

In order to solve the above integral equations, the extended finite element method is employed here to obtain the values of $\mathbf{u}(\mathbf{x}, t)$ and $p_w(\mathbf{x}, t)$. To achieve this aim, the displacement and pressure fields are enriched based on the analytical solution to make the approximations capable of tracking the discontinuities. Various enrichment functions can be used to enhance the approximation fields. The level set method is generally used to model the material interfaces, while the Heaviside step function is more applicable to crack problems. In this study, the level set function is employed to enhance the FEM approximation for problems containing the material interfaces.

The enriched approximation of the extended finite element method for field variable $\varphi(\boldsymbol{x})$ can be written as

$$\varphi^h(\boldsymbol{x}) = \sum_{i=1}^{n} N_i(\boldsymbol{x})\bar{\varphi}_i + \sum_{J=1}^{M}\left(\sum_{i=1}^{n} N_i(\boldsymbol{x})\left(\psi^J(\boldsymbol{x}) - \bar{\psi}_i^J(\boldsymbol{x})\right)\bar{a}_i^J\right), \tag{11}$$

where $N_i(\boldsymbol{x})$ is the standard FE shape function, n is the number of element nodes, M is the number of interfaces cut the element, $\psi^J(\boldsymbol{x})$ is an appropriate enrichment function of the Jth interface, and $\bar{a}_i^J$ is the additional degrees-of-freedom due to interface J of enriched node i. The above enriched field can be used in all elements cut by the interfaces. To model the weak discontinuities, such as the material interfaces, the level set distance function is used as the enrichment function, which is defined as

$$\psi^J(\boldsymbol{x}) = \min\left\|\boldsymbol{x} - \widehat{\boldsymbol{x}}^J\right\|\mathrm{sign}\left(\mathbf{n}^J \cdot \left(\boldsymbol{x} - \widehat{\boldsymbol{x}}^J\right)\right), \tag{12}$$

where $\widehat{\boldsymbol{x}}^J$ is the point on the Jth interface, $\mathbf{n}^J$ is the normal vector to the interface J at the point $\widehat{\boldsymbol{x}}^J$, and $\boldsymbol{x}$ is an arbitrary point of the domain.

3.1. The X-FEM discretization

The discrete form of integral Eq. (10) can be obtained for the extended finite element model by using the following test and trial functions for the displacement and pressure fields. Applying the enriched field (11), the trial functions $\mathbf{u}(\boldsymbol{x},t)$ and $p_w(\boldsymbol{x},t)$ can be defined as

$$\mathbf{u}(\boldsymbol{x}) \approx \mathbf{u}^h(\boldsymbol{x}) = \sum_{i=1}^{n_u}\left(N_{\mathrm{std}}^u\right)_i(\boldsymbol{x})\bar{\mathbf{u}}_i + \sum_{J=1}^{M}\left(\sum_{i=1}^{n_u}\left(N_{\mathrm{std}}^u\right)_i(\boldsymbol{x})\left(\psi^J(\boldsymbol{x}) - \bar{\psi}_i^J(\boldsymbol{x})\right)\bar{\mathbf{a}}_i^J\right),$$
$$p_w(\boldsymbol{x}) \approx p_w^h(\boldsymbol{x}) = \sum_{i=1}^{n_p}\left(N_{\mathrm{std}}^p\right)_i(\boldsymbol{x})\bar{p}_{w_i} + \sum_{J=1}^{M}\left(\sum_{i=1}^{n_p}\left(N_{\mathrm{std}}^p\right)_i(\boldsymbol{x})\left(\psi^J(\boldsymbol{x}) - \bar{\psi}_i^J(\boldsymbol{x})\right)\bar{b}_i^J\right). \tag{13}$$

The above relations can be simply shown as $\mathbf{u}(\boldsymbol{x}) = \mathbf{N}_{\mathrm{std}}^u\bar{\mathbf{u}} + \mathbf{N}_{\mathrm{enr}}^u\bar{\mathbf{a}}$ and $p_w(\boldsymbol{x}) = \mathbf{N}_{\mathrm{std}}^p\bar{\mathbf{p}}_w + \mathbf{N}_{\mathrm{enr}}^p\bar{\mathbf{b}}$. The test functions $\delta\mathbf{u}(\boldsymbol{x},t)$ and $\delta p_w(\boldsymbol{x},t)$ can be also defined as

$$\delta\mathbf{u}^h(\boldsymbol{x}) = \sum_{i=1}^{n_u}\left(N_{\mathrm{std}}^u\right)_i(\boldsymbol{x})\delta\bar{\mathbf{u}}_i + \sum_{J=1}^{M}\left(\sum_{i=1}^{n_u}\left(N_{\mathrm{std}}^u\right)(\boldsymbol{x})\left(\psi^J(\boldsymbol{x}) - \bar{\psi}_i^J(\boldsymbol{x})\right)\delta\bar{\mathbf{a}}_i^J\right),$$
$$\delta p_w^h(\boldsymbol{x}) = \sum_{i=1}^{n_p}\left(N_{\mathrm{std}}^p\right)_i(\boldsymbol{x})\delta\bar{p}_{w_i} + \sum_{J=1}^{M}\left(\sum_{i=1}^{n_p}\left(N_{\mathrm{std}}^p\right)_i(\boldsymbol{x})\left(\psi^J(\boldsymbol{x}) - \bar{\psi}_i^J(\boldsymbol{x})\right)\delta\bar{b}_i^J\right), \tag{14}$$

where $\psi^J(\boldsymbol{x})$ is the signed distance function with respect to the interface J, as given by relation (12). The matrix form of the enhanced element shape functions can be written as $\mathbf{N}_{\mathrm{enhanced}}^u = [\mathbf{N}_{\mathrm{std}}^u, \mathbf{N}_{\mathrm{enr}}^u]$ and $\mathbf{N}_{\mathrm{enhanced}}^p = [\mathbf{N}_{\mathrm{std}}^p, \mathbf{N}_{\mathrm{enr}}^p]$, in which $\mathbf{N}_{\mathrm{std}}^u$ and $\mathbf{N}_{\mathrm{std}}^p$ are the standard displacement and pressure shape functions, and $\mathbf{N}_{\mathrm{enr}}^u$ and $\mathbf{N}_{\mathrm{enr}}^p$ are the enriched displacement and pressure shape functions defined as $(N_{\mathrm{enr}}^u)_i = (N_{\mathrm{std}}^u)_i(\psi - \bar{\psi}_i)$ and $(N_{\mathrm{enr}}^p)_i = (N_{\mathrm{std}}^p)_i(\psi - \bar{\psi}_i)$. Similarly, the derivatives of displacement shape functions can be defined by $\mathbf{B}_{\mathrm{enhanced}}^u = [\mathbf{B}_{\mathrm{std}}^u, \mathbf{B}_{\mathrm{enr}}^u]$, with $(B_{\mathrm{std}}^u)_{ji} = \partial(N_{\mathrm{std}}^u)_i/\partial x_j$ and $(B_{\mathrm{enr}}^u)_{ji} = \partial(N_{\mathrm{enr}}^u)_i/\partial x_j$.

Substituting the trial and test functions (13) and (14) into the weak form of governing Eq. (10) and considering the arbitrariness of displacement and pressure variations, the following discrete set of coupled equations can be obtained as

$$\begin{pmatrix} \mathbf{M}_{uu} & \mathbf{M}_{ua} \\ \mathbf{M}_{au} & \mathbf{M}_{aa} \end{pmatrix}\begin{Bmatrix} \ddot{\bar{\mathbf{u}}} \\ \ddot{\bar{\mathbf{a}}} \end{Bmatrix} + \begin{pmatrix} \mathbf{K}_{uu} & \mathbf{K}_{ua} \\ \mathbf{K}_{au} & \mathbf{K}_{aa} \end{pmatrix}\begin{Bmatrix} \bar{\mathbf{u}} \\ \bar{\mathbf{a}} \end{Bmatrix} - \begin{pmatrix} \mathbf{Q}_{up} & \mathbf{Q}_{ub} \\ \mathbf{Q}_{ap} & \mathbf{Q}_{ab} \end{pmatrix}\begin{Bmatrix} \bar{\mathbf{p}}_w \\ \bar{\mathbf{b}} \end{Bmatrix} - \begin{Bmatrix} \mathbf{f}_u^{(1)} \\ \mathbf{f}_a^{(1)} \end{Bmatrix} = \mathbf{0},$$

$$\begin{pmatrix} \widetilde{\mathbf{Q}}_{pu} & \widetilde{\mathbf{Q}}_{pa} \\ \widetilde{\mathbf{Q}}_{bu} & \widetilde{\mathbf{Q}}_{ba} \end{pmatrix}\begin{Bmatrix} \dot{\bar{\mathbf{u}}} \\ \dot{\bar{\mathbf{a}}} \end{Bmatrix} + \begin{pmatrix} \mathbf{H}_{pp} & \mathbf{H}_{pb} \\ \mathbf{H}_{bp} & \mathbf{H}_{bb} \end{pmatrix}\begin{Bmatrix} \bar{\mathbf{p}}_w \\ \bar{\mathbf{b}} \end{Bmatrix} + \begin{pmatrix} \widetilde{\mathbf{S}}_{pp} & \widetilde{\mathbf{S}}_{pb} \\ \widetilde{\mathbf{S}}_{bp} & \widetilde{\mathbf{S}}_{bb} \end{pmatrix}\begin{Bmatrix} \dot{\bar{\mathbf{p}}}_w \\ \dot{\bar{\mathbf{b}}} \end{Bmatrix} - \begin{Bmatrix} \mathbf{f}_p^{(2)} \\ \mathbf{f}_b^{(2)} \end{Bmatrix} = \mathbf{0}, \tag{15}$$

where

$$\mathbf{M}_{\alpha\beta} = \int_{\Omega}\left(\mathbf{N}_{\alpha}^u\right)^T\rho\mathbf{N}_{\beta}^u d\Omega,$$

$$\mathbf{K}_{\alpha\beta} = \int_{\Omega}\left(\mathbf{B}_{\alpha}^u\right)^T\mathbf{D}\mathbf{B}_{\beta}^u d\Omega,$$

$$\mathbf{Q}_{\alpha\gamma} = \int_{\Omega}\left(\mathbf{B}_{\alpha}^u\right)^T S_w\alpha\mathbf{m}\mathbf{N}_{\gamma}^p d\Omega, \tag{16}$$

$$\mathbf{f}_{\alpha}^{(1)} = \int_{\Omega}\left(\mathbf{N}_{\alpha}^u\right)^T\rho\mathbf{b}d\Omega + \int_{\Gamma}\left(\mathbf{N}_{\alpha}^u\right)^T\bar{\mathbf{t}}\,d\Gamma$$

and

$$\widetilde{\mathbf{Q}}_{\delta\alpha} = \int_{\Omega} (\mathbf{N}^p_{\delta})^T S_w \alpha \mathbf{m}^T \mathbf{B}^u_{\alpha} \, d\Omega,$$

$$\mathbf{H}_{\delta\gamma} = \int_{\Omega} (\nabla\mathbf{N}^p_{\delta})^T \mathbf{k}(\nabla\mathbf{N}^p_{\gamma}) d\Omega,$$

$$\widetilde{\mathbf{S}}_{\delta\gamma} = \int_{\Omega} (\mathbf{N}^p_{\delta})^T \frac{1}{Q^*} \mathbf{N}^p_{\gamma} d\Omega,$$

$$\mathbf{f}^{(2)}_{\delta} = \int_{\Gamma} (\mathbf{N}^p_{\delta})^T \tilde{q}_n d\Gamma - \int_{\Omega} (\nabla\mathbf{N}^p_{\delta})^T \mathbf{k} S_w \rho_f \mathbf{b} \, d\Omega,$$

(17)

where $\mathbf{N}^u_{(\alpha,\beta)} = \mathbf{N}^u_{(\text{std,enr})}, \mathbf{N}^p_{(\gamma,\delta)} = \mathbf{N}^p_{(\text{std,enr})}$ and $\mathbf{B}^u_{(\alpha,\beta)} = \mathbf{B}^u_{(\text{std,enr})}$, in which $\bar{\mathbf{u}}$ and $\bar{\mathbf{p}}_w$ refers to the standard displacement and pressure DOFs, and $\bar{\mathbf{a}}$ and $\bar{\mathbf{b}}$ refers to the additional degrees-of-freedom of displacement and pressure variables. In above equations, $\mathbf{m}$ is the vector of Dirac delta function defined as $\mathbf{m}^T = \langle 1\ 1\ 0 \rangle$. The X-FEM discretization Eq. (15) can be rewritten as

$$\mathbf{M}\ddot{\overline{\mathbb{U}}} + \mathbf{K}\overline{\mathbb{U}} - \mathbf{Q}\overline{\mathbb{P}} - \mathbf{F}^{(1)} = \mathbf{0},$$

$$\widetilde{\mathbf{Q}}\dot{\overline{\mathbb{U}}} + \mathbf{H}\overline{\mathbb{P}} + \widetilde{\mathbf{S}}\dot{\overline{\mathbb{P}}} - \mathbf{F}^{(2)} = \mathbf{0},$$

(18)

where $\overline{\mathbb{U}} = \langle \bar{\mathbf{u}}, \bar{\mathbf{a}} \rangle$ and $\overline{\mathbb{P}} = \langle \bar{\mathbf{p}}_w, \bar{\mathbf{b}} \rangle$ are the complete set of the standard and enriched degrees-of-freedom of displacement and pressure fields, respectively.

3.2. The time domain discretization

In order to complete the numerical solution of FE equations, it is necessary to integrate the time differential Eq. (18) in time. The generalized Newmark GN22 method is employed for the displacement field $\overline{\mathbb{U}}$ and GN11 method for the pressure field $\overline{\mathbb{P}}$ as [47]

$$\ddot{\overline{\mathbb{U}}}^{t+\Delta t} = \ddot{\overline{\mathbb{U}}}^t + \Delta\ddot{\overline{\mathbb{U}}}^t,$$

$$\dot{\overline{\mathbb{U}}}^{t+\Delta t} = \dot{\overline{\mathbb{U}}}^t + \ddot{\overline{\mathbb{U}}}^t\Delta t + \beta_1\Delta\ddot{\overline{\mathbb{U}}}^t\Delta t,$$

$$\overline{\mathbb{U}}^{t+\Delta t} = \overline{\mathbb{U}}^t + \dot{\overline{\mathbb{U}}}^t\Delta t + \frac{1}{2}\ddot{\overline{\mathbb{U}}}^t\Delta t^2 + \frac{1}{2}\beta_2\Delta\ddot{\overline{\mathbb{U}}}^t\Delta t^2$$

(19)

and

$$\dot{\overline{\mathbb{P}}}^{t+\Delta t} = \dot{\overline{\mathbb{P}}}^t + \Delta\dot{\overline{\mathbb{P}}}^t,$$

$$\overline{\mathbb{P}}^{t+\Delta t} = \overline{\mathbb{P}}^t + \dot{\overline{\mathbb{P}}}^t\Delta t + \bar{\beta}\Delta\dot{\overline{\mathbb{P}}}^t\Delta t,$$

(20)

where β_1, β_2 and $\bar{\beta}$ are parameters, which are usually chosen in the range of 0–1. However, for unconditionally stability of the algorithm, it is required that $\beta_1 \geqslant \beta_2 \geqslant \frac{1}{2}$ and $\bar{\beta} \geqslant \frac{1}{2}$. In above relations, $\overline{\mathbb{U}}^t, \dot{\overline{\mathbb{U}}}^t$ and $\ddot{\overline{\mathbb{U}}}^t$ denote the known values of displacement, velocity and acceleration of the standard and enriched degrees of freedom at time t, and $\overline{\mathbb{P}}^t$ and $\dot{\overline{\mathbb{P}}}^t$ are the known values of pressure and gradient of pressure of the standard and enriched DOFs at time t. Substituting relations 19) and (20) into the space-discrete Eq. (18), the following nonlinear equation can be achieved as

$$\begin{pmatrix} \mathbf{M}_{uu} + \frac{1}{2}\beta_2\Delta t^2\mathbf{K}_{uu} & \mathbf{M}_{ua} + \frac{1}{2}\beta_2\Delta t^2\mathbf{K}_{ua} & -\bar{\beta}\Delta t\mathbf{Q}_{up} & -\bar{\beta}\Delta t\mathbf{Q}_{ub} \\ \mathbf{M}_{au} + \frac{1}{2}\beta_2\Delta t^2\mathbf{K}_{au} & \mathbf{M}_{aa} + \frac{1}{2}\beta_2\Delta t^2\mathbf{K}_{aa} & -\bar{\beta}\Delta t\mathbf{Q}_{ap} & -\bar{\beta}\Delta t\mathbf{Q}_{ab} \\ \beta_1\Delta t\widetilde{\mathbf{Q}}_{pu} & \beta_1\Delta t\widetilde{\mathbf{Q}}_{pa} & \widetilde{\mathbf{S}}_{pp} + \bar{\beta}\Delta t\mathbf{H}_{pp} & \widetilde{\mathbf{S}}_{pb} + \bar{\beta}\Delta t\mathbf{H}_{pb} \\ \beta_1\Delta t\widetilde{\mathbf{Q}}_{bu} & \beta_1\Delta t\widetilde{\mathbf{Q}}_{ba} & \widetilde{\mathbf{S}}_{bp} + \bar{\beta}\Delta t\mathbf{H}_{bp} & \widetilde{\mathbf{S}}_{bb} + \bar{\beta}\Delta t\mathbf{H}_{bb} \end{pmatrix} \begin{Bmatrix} \Delta\ddot{\bar{\mathbf{u}}}^t \\ \Delta\ddot{\bar{\mathbf{a}}}^t \\ \Delta\dot{\bar{\mathbf{p}}}^t_w \\ \Delta\dot{\bar{\mathbf{b}}}^t \end{Bmatrix} = \begin{Bmatrix} \mathbf{G}^{(1)}_u \\ \mathbf{G}^{(1)}_a \\ \mathbf{G}^{(2)}_p \\ \mathbf{G}^{(2)}_b \end{Bmatrix},$$

(21)

where the right-hand-side of above equation denotes the vector of known values at time t defined as

$$\mathbb{G}^{(1)} = \left\langle \mathbf{G}^{(1)}_u \quad \mathbf{G}^{(1)}_a \right\rangle^T = {}^{t+\Delta t}\mathbf{F}^{(1)} - \mathbf{M}\ddot{\overline{\mathbb{U}}}^t - \mathbf{K}\left(\overline{\mathbb{U}}^t + \dot{\overline{\mathbb{U}}}^t\Delta t + \frac{1}{2}\ddot{\overline{\mathbb{U}}}^t\Delta t^2\right) + \mathbf{Q}\left(\overline{\mathbb{P}}^t + \dot{\overline{\mathbb{P}}}^t\Delta t\right),$$

$$\mathbb{G}^{(2)} = \left\langle \mathbf{G}^{(2)}_p \quad \mathbf{G}^{(2)}_b \right\rangle^T = {}^{t+\Delta t}\mathbf{F}^{(2)} - \widetilde{\mathbf{Q}}\left(\dot{\overline{\mathbb{U}}}^t + \ddot{\overline{\mathbb{U}}}^t\Delta t\right) - \mathbf{H}\left(\overline{\mathbb{U}}^t + \dot{\overline{\mathbb{U}}}^t\Delta t\right) - \widetilde{\mathbf{S}}\dot{\overline{\mathbb{P}}}^t.$$

(22)

Eq. (21) can be therefore simplified as

$$\begin{pmatrix} \mathbf{M} + \frac{1}{2}\beta_2\Delta t^2\mathbf{K} & -\bar{\beta}\Delta t\mathbf{Q} \\ \beta_1\Delta t\widetilde{\mathbf{Q}} & \widetilde{\mathbf{S}} + \bar{\beta}\Delta t\mathbf{H} \end{pmatrix} \begin{Bmatrix} \Delta\ddot{\overline{\mathbb{U}}}^t \\ \Delta\dot{\overline{\mathbb{P}}}^t \end{Bmatrix} = \begin{Bmatrix} \mathbb{G}^{(1)} \\ \mathbb{G}^{(2)} \end{Bmatrix}.$$

(23)

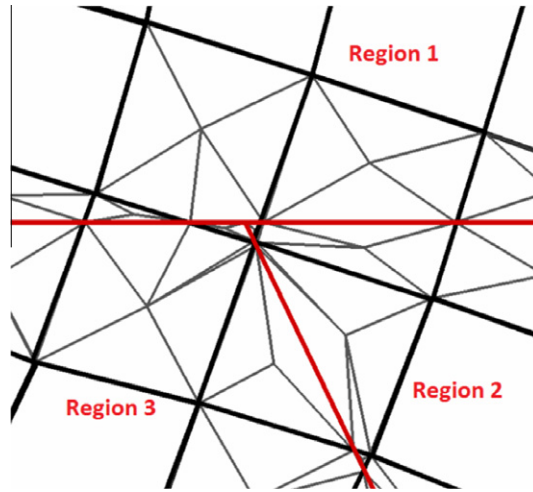The set of nonlinear Eq. (23) can be solved using an appropriate approach, such as the Newton–Raphson procedure.

Fig. 1. The sub-triangles associated with elements cut by interfaces with different internal regions.

3.3. Computational notes

For the elements cut by the interface, the standard Gauss quadrature points are insufficient for numerical integration, and may not adequately integrate the interface boundary. Thus, it is necessary to modify the element quadrature points to accurately evaluate the contribution to the weak form for both sides of interface. In the standard FE method, the numerical integration can be performed by discretizing the domain as $\Omega = \cup_{e=1}^{m} \Omega_e$, in which m is the number of elements and Ω_e is the element sub-domain. In X-FEM, the elements located on interface boundary can be partitioned by triangular sub-domains Ω_s with the boundaries aligned with the material interface, i.e. $\Omega_e = \cup_{s=1}^{m_s} \Omega_s$, in which m_s denotes the number of sub-triangles of the element (Fig. 1). The numerical integration of enriched elements can be performed over these new sub-triangles using the standard Gauss quadrature points. It is important that the Gauss points of sub-triangles are only used for the numerical integration of the elements cut by the interface and no new degrees-of-freedom are added to the system.

The proposed computational model presented in preceding section is capable of considering any number of material interfaces for an enriched element. In this case, it is only required to apply an efficient technique for obtaining the elements located on material interfaces and the material properties of corresponding integration points. In the literature, it was suggested to use the sign of distance function in order to obtain the material properties of each integration point, however, it is not simple for an element cut by various interfaces. In this study, an efficient technique is developed based on the Gauss point position in *polygon routines*, which can be simply used to determine the material property of each Gauss point in an enriched element with several material interfaces. It must be noted that the position of each sample point is computed in the local coordinates of the element, so it is not required to update its position in global coordinates. In order to obtain the local coordinates of each sample point of triangular sub-domain, the following nonlinear equations must be solved using the global coordinates as

$$
\begin{aligned}
f_1(\xi,\eta) &= x_p - \sum_i N_i(\xi,\eta)\bar{x}_i = 0, \\
f_2(\xi,\eta) &= y_p - \sum_i N_i(\xi,\eta)\bar{y}_i = 0,
\end{aligned}
\tag{24}
$$

where (x_p, y_p) is the global coordinates of sample point. This nonlinear equation can be solved using the Newton–Raphson procedure as

$$
\begin{Bmatrix} \xi^{k+1} \\ \eta^{k+1} \end{Bmatrix} = \begin{Bmatrix} \xi^k \\ \eta^k \end{Bmatrix} - \begin{bmatrix} \frac{\partial f_1^k}{\partial \xi} & \frac{\partial f_1^k}{\partial \eta} \\ \frac{\partial f_2^k}{\partial \xi} & \frac{\partial f_2^k}{\partial \eta} \end{bmatrix}^{-1} \begin{Bmatrix} f_1(\xi^k,\eta^k) \\ f_2(\xi^k,\eta^k) \end{Bmatrix}.
\tag{25}
$$

4. Numerical simulation results

In order to illustrate the accuracy and versatility of the extended finite element method in deformable porous media, several numerical examples of elastic soil column, elastic foundation, and the lower San–Fernando dam are presented. The first two examples are chosen to assess the accuracy of the X-FEM model for two dynamic problems of fully saturated media. The last example presents the plasticity analysis of the lower San Fernando dam under the earthquake of 1971. The examples are

solved using both FEM and X-FEM techniques, and the results are compared. In order to perform a real comparison, the number of elements in FEM and X-FEM meshes are taken almost equal. In all three examples, a uniform X-FEM mesh is used independent of the shape of material interfaces, while the FEM mesh is conformed to the geometry of interface. All examples are simulated by a plain strain representation and the convergence tolerance is set to 10^{-8}.

4.1. Elastic soil column

The first example is a fully saturated soil column subjected to a surface step loading, which is solved by the X-FEM and the results are compared with those of FEM model. The column has a width of $w = 1.0$ m and a height of $H = 30$ m, which is subjected to a surface step loading of 1 kN/m² applied in 0.1 s with a fixed pore pressure of $p = 0$ at the top of column. The geometry and boundary conditions of soil column is shown in Fig. 2, and the material properties are summarized in Table 1. The problem includes two regions with a horizontal material interface, as shown in this figure. The mesh consists of 10 four-noded quadrilateral elements for both displacement and pressure fields. The generalized Newmark GN22 method is employed for the standard and enriched displacement DOFs and the GN11 method for the standard and enriched DOFs of pressure. The time step is set to 0.05 s. The FEM and X-FEM meshes are shown in Fig. 2. The variations with time of pore pressure are plotted in Fig. 3 at four points of column, i.e. points 3, 7, 15 and 19. As can be seen from this figure, the proposed dynamic X-FEM simulation is in good agreement with those obtained by FEM. Also plotted in Fig. 4 are the variations with time of the vertical displacement at points 17 and 21. Good agreement can be observed between the FEM and X-FEM models.

4.2. Elastic foundation

The second example is an elastic foundation subjected to a surface step loading with three internal sub-domains. The foundation problem is one of the most popular examples used by various researchers to capture the shear band localization [48]. In this study, a fully saturated soil foundation with a step loading of 350 kN/m² is applied in 0.1 s and, a fixed pore pres-
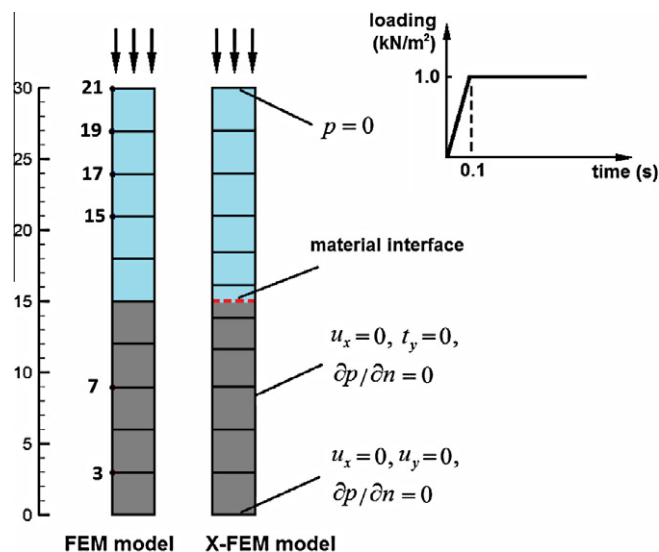

Fig. 2. Soil column subjected to a surface step loading; The geometry and boundary condition together with the X-FEM and FEM meshes.

Table 1
Soil column; material properties.

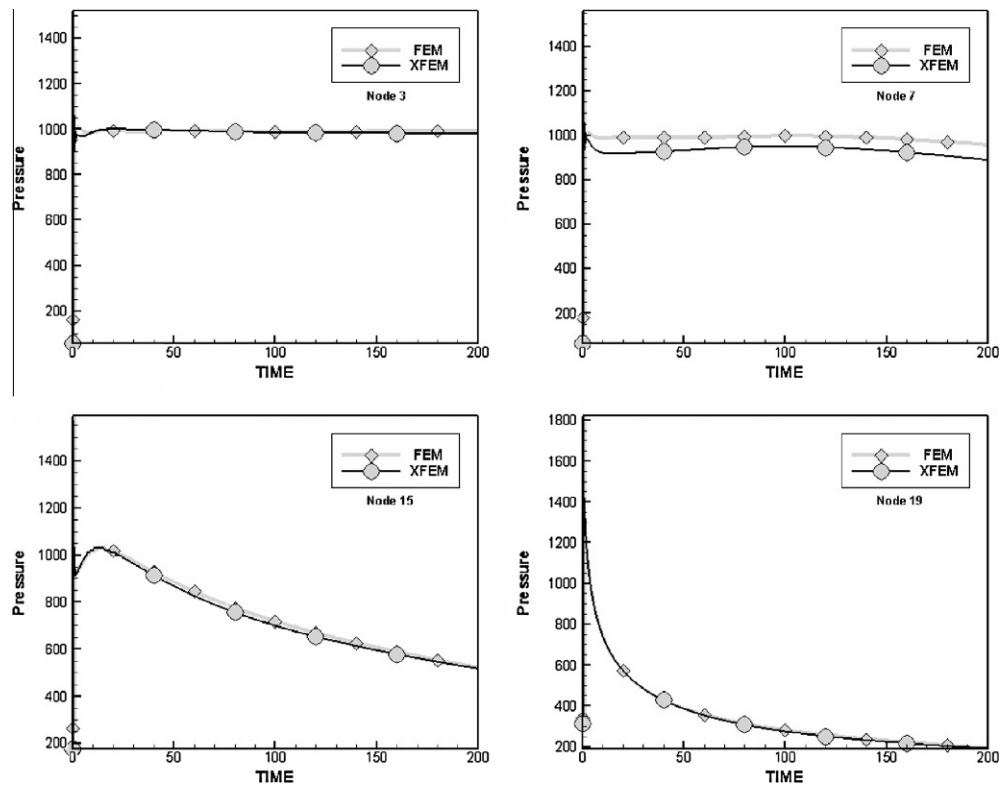| Material properties	Region 1	Region 2
E (Pa)	3.0e−7	6.0e−7
υ	0.2	0.2
ρ_s (kg/m³)	2000	2000
ρ_f (kg/m³)	1000	1000
K_f (Pa)	2.1e−9	2.1e−9
K_s (Pa)	1.0e−20	1.0e−20
n	0.3	0.3
k (m³s/kg)	1.02e−8	1.02e−9

Fig. 3. Soil column; the pressure history of FEM and X-FEM models at different nodes.
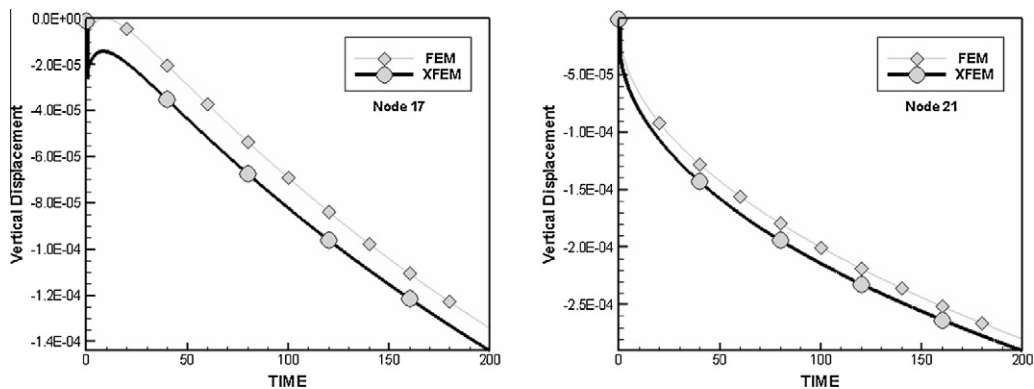

Fig. 4. Soil column; the displacement history of FEM and X-FEM models at different nodes.

sure of $p = 0$ is assumed at the top of foundation. The foundation is 30×30 m with the geometry and boundary conditions shown in Fig. 5. The material properties of foundation for three regions are given in Table 2. The four-noded quadrilateral elements are used for both displacement and pressure fields in the FEM and X-FEM analyzes. The time step is set to 0.01 s. In finite element simulation, the FE mesh is conformed to the boundary of material interfaces, while in X-FEM analysis the interfaces pass through the elements. In the X-FEM model, a partitioning procedure is used to generate the sub-triangles. For those elements cut by the interfaces, the Gauss points of sub-triangles are then employed to evaluate the stiffness, mass, compressibility, and permeability matrices. The variations with time of pore pressure are plotted in Fig. 6 at four points of foundation. Remarkable agreement can be seen between the X-FEM and FEM dynamic simulations. In Fig. 7, the variations with time of the vertical displacement are plotted at different points, which are in good agreement with those obtained by the FEM analyzes. Finally, the distributions of pressure contour are shown in Fig. 8 at $t = 1.0$ and 10.0 s using the FEM and X-FEM models. A good agreement can be observed between two techniques.
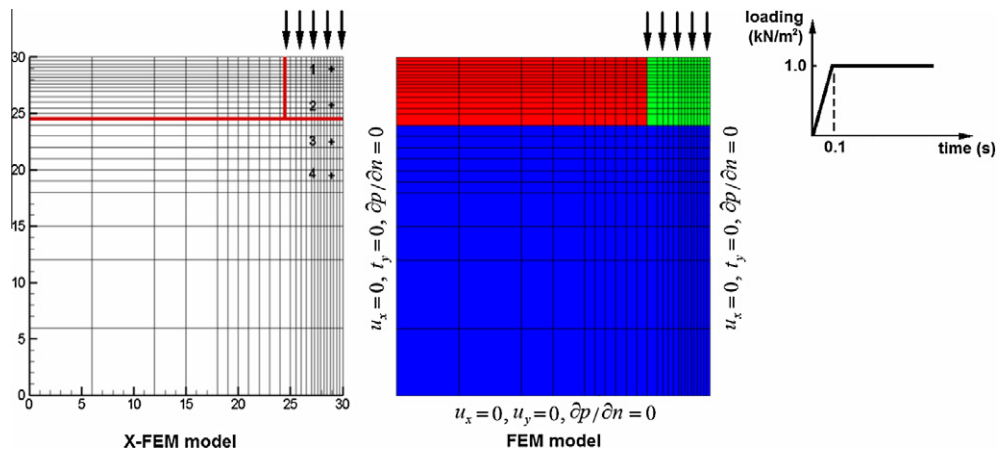
Fig. 5. Elastic foundation subjected to a surface step loading; The geometry and boundary condition together with the X-FEM and FEM meshes.

Table 2
Elastic foundation; material properties.

Material properties	Region 1	Region 2	Region 3
E (Pa)	20.0e−6	40.0e−6	100.0e−6
υ	0.2	0.2	0.2
ρ_s (kg/m^3)	2000	2000	2000
ρ_f (kg/m^3)	1000	1000	1000
K_f(Pa)	2.1e−9	2.1e−9	2.1e−9
K_s (Pa)	1.0e−20	1.0e−20	1.0e−20
n	0.25	0.3	0.35
k (m^{3}s/kg)	1.00e−8	5.00e−8	2.00e−7

4.3. The lower San–Fernando dam

The last example demonstrates the performance of X-FEM model in elasto-plastic analysis of saturated and unsaturated earth dam. The analysis is performed to simulate the lower San Fernando dam in steady state condition. The dam was collapsed during the earthquake of February 9, 1971. Although the earthquake lasted for about 15 s, the failure of dam occurred at about 60 s after beginning of the earthquake. The time difference between the failure and end of the earthquake was due to important pore pressure build-up, as a result of cyclic loading, first in the central portion of the dam and then, the migration of this excess pore pressure in the post earthquake period to the regions closer to the upstream slope of the dam, and so the failure occurred at about 60 s after beginning of the earthquake. In this study, the performance of X-FEM model is illustrated in a practical complex geometry of earth and rockfill dam. In order to adequately produce the soil behavior under complicated loading conditions, the modified Pastor–Zienkiewicz generalized plasticity model is employed here. This model was originally developed by Pastor et al. [49] for fully saturated soils and then extended to partially saturated soils by Zhang et al. [50]. The details of modified Pastor–Zienkiewicz model are given in Appendix A.

The geometry, material zones and boundary conditions of the dam are shown in Fig. 9. Also presented in this figure is the FEM and X-FEM meshes used in the analyses for both solid and fluid phases. The general material properties of the dam are given in Table 3 for different zones. The material parameters of modified Pastor–Zienkiewicz model are listed in Table 4 [51,52]. The time step is set to 0.001 s. The distribution of pore pressure in the dam body at steady state condition is presented in Fig. 10(a) for the FEM and X-FEM techniques. As can be observed, the negative pore pressure exists in the dam crest and downstream slope in unsaturated zones. Also presented in Fig. 10(b)–(d) are the distributions of effective vertical stress, shear stress and vertical displacement contours in the dam body at steady state condition using two different techniques.

In Fig. 11, the variations of excess pore pressure with time are shown at different nodes using the FEM and X-FEM models. Obviously, both techniques evaluate the peak of excess pore pressure after the end of earthquake, and the larger value of water pore pressure at the center portion of the dam, i.e. node 3. In Fig. 12, the variations of vertical displacement with time are presented at the dam crest and upstream slope. It can be observed from the results of displacements that the higher value of deformation occurs in the upstream slope and, causes the failure in this region near the center of the dam. In order to illustrate the mechanism of the failure in the dam body, the distribution of excess pore water pressure and the effective stress contours are presented in Figs. 13 and 14 at 25 and 50 s after beginning of the earthquake. According to Fig. 13, there is a region with larger excess water pressure in the center of the dam. However, this excess water pressure moves from the center into the upstream slope of the dam, as shown in Fig. 14, which is similar to the failure surface of the dam occurred in
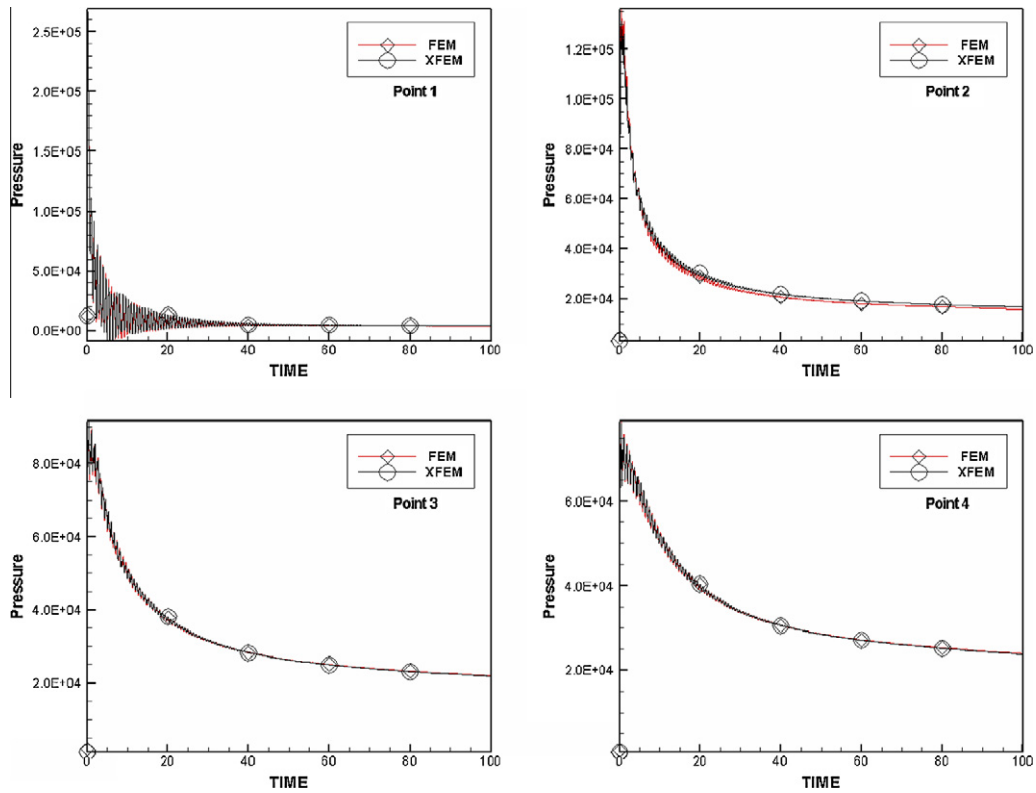
Fig. 6. Elastic foundation; the pressure history of FEM and X-FEM models at different nodes.
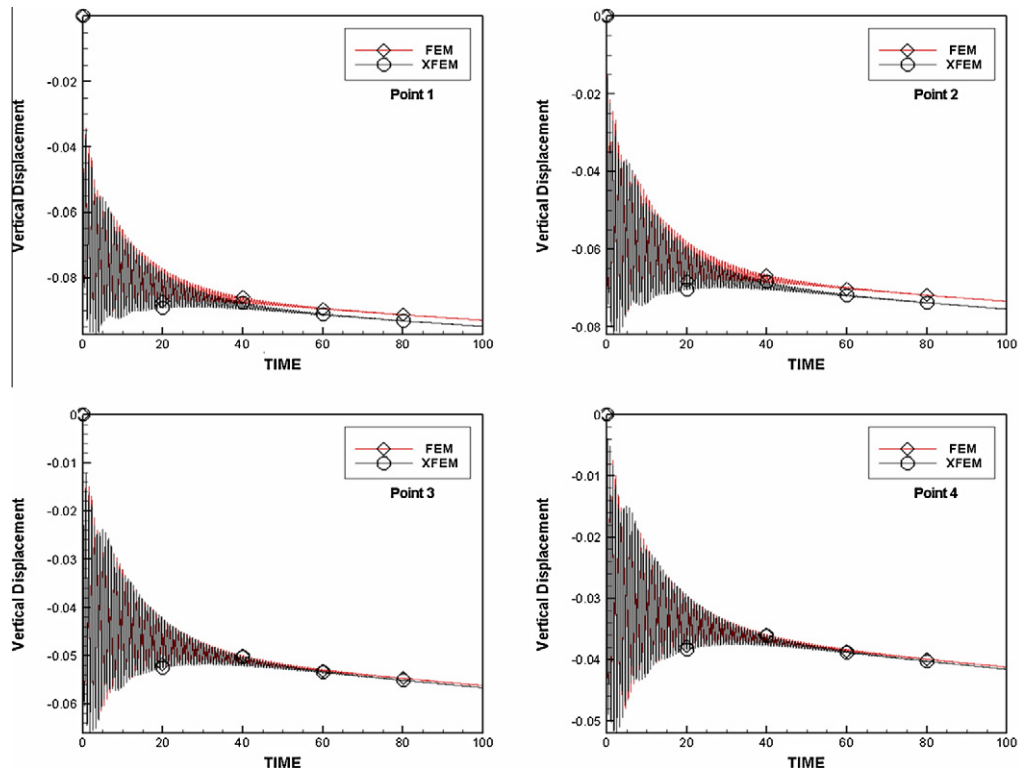

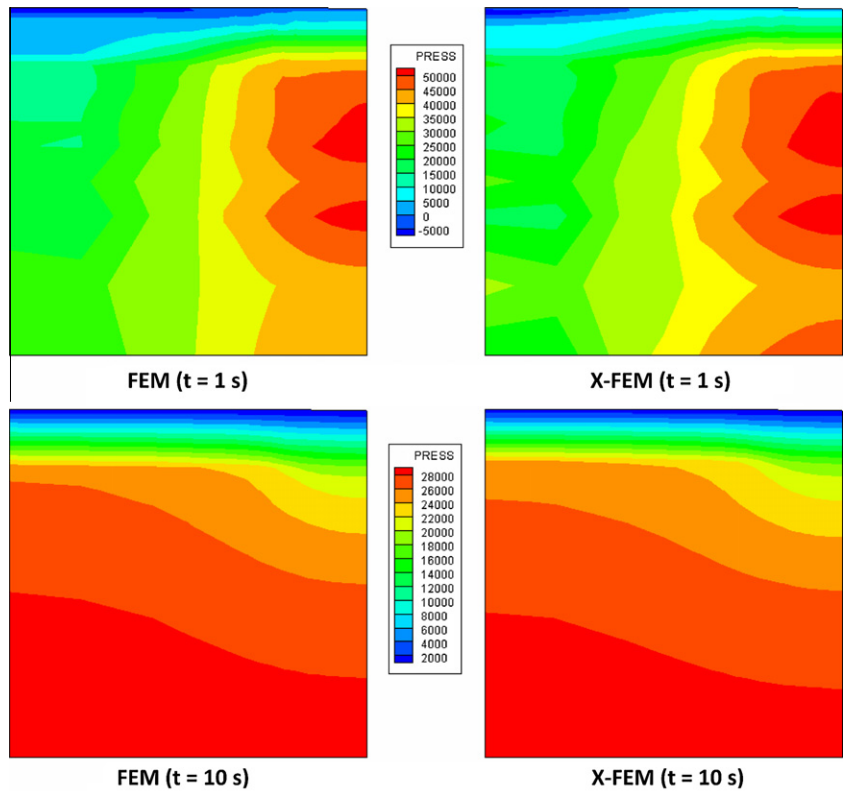**Fig. 7.** Elastic foundation; the displacement history of FEM and X-FEM models at different nodes.

Fig. 8. Elastic foundation; the distribution of pressure contours using the FEM and X-FEM models at t = 1 and 10 s.
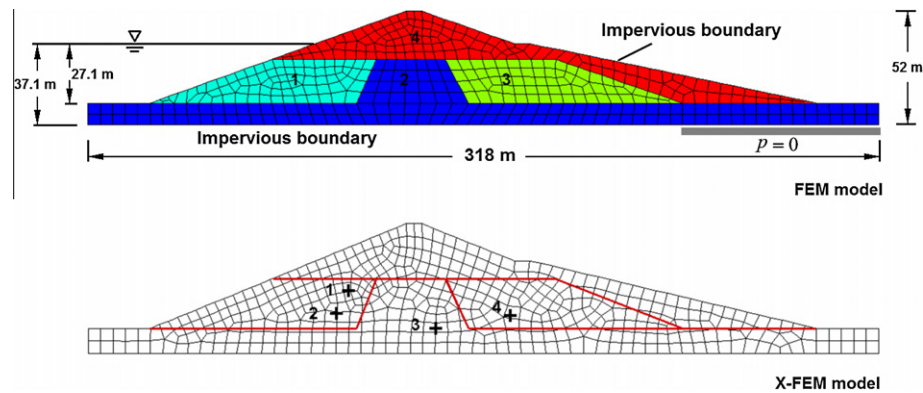

Fig. 9. The lower San–Fernando dam; The material zones and the FEM and X-FEM meshes.

Table 3
The lower San Fernando dam, elastic material properties.

Material properties	Region 1	Region 2	Region 3	Region 4
E (Pa)	1.53e−8	0.893e−8	0.96e−8	1.02e−8
υ	0.2857	0.2857	0.2857	0.2857
ρ_s (kg/m³)	2756.0	2644.0	2644.0	2644.0
ρ_f (kg/m³)	980.0	980.0	980.0	980.0
K_f (Pa)	2.0e−9	2.0e−9	2.0e−9	2.0e−9
K_s (Pa)	1.0e−22	1.0e−22	1.0e−22	1.0e−22
n	0.375	0.375	0.375	0.375
k (m³s/kg)	1.0e−7	1.0e−6	1.0e−6	1.0e−7

Table 4
The lower San Fernando dam, Pastor–Zienkiewicz material properties.

Material properties	Region 1	Region 2	Region 3	Region 4
M_g	1.51	1.51	1.51	1.51
M_f	1.4	0.775	0.906	1.01325
α_f	0.45	0.45	0.45	0.45
α_g	0.45	0.45	0.45	0.45
K_{eV0}	120.0	70.0	75.0	80.0
K_{es0}	180.0	105.0	112.0	120.0
β_0	4.2	4.2	4.2	4.2
β_1	0.2	0.2	0.2	0.2
H_0	7.0e−2	4.083e−2	4.375e−2	4.67e−2
H_{u0} (Pa)	0.6e−8	0.35e−8	0.375e−8	0.4e−8
γ_u	2.0	2.0	2.0	2.0
γ	2.0	2.0	2.0	2.0
$p_{cut-off}$ (Pa)	2.0e−3	2.0e−3	2.0e−3	2.0e−3
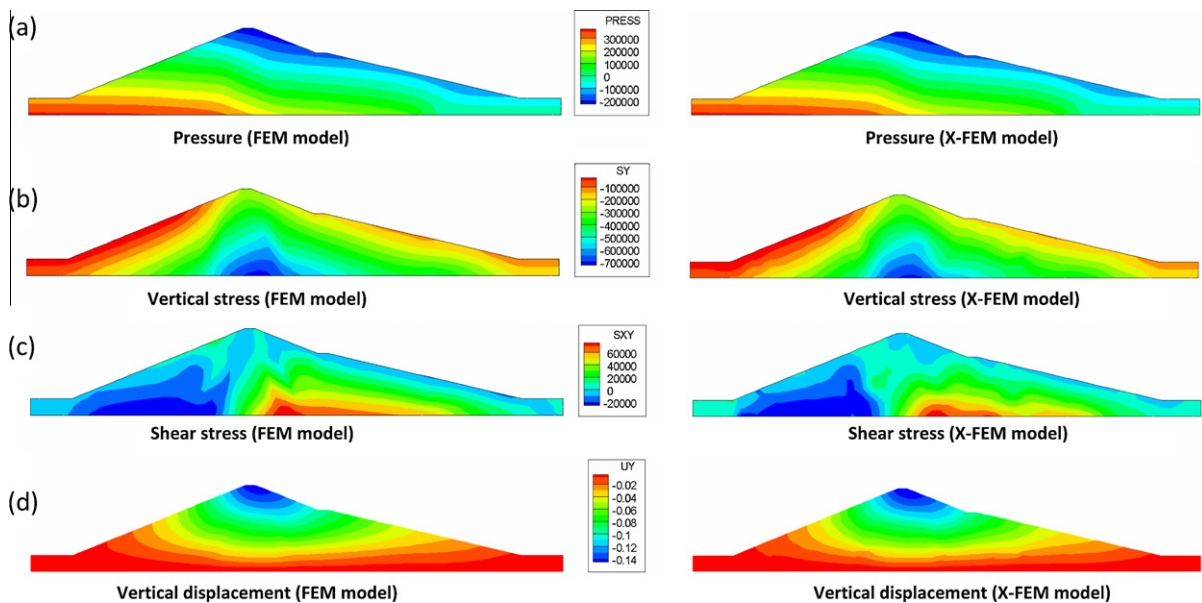
Fig. 10. Numerical simulation of the steady state condition for the lower San–Fernando dam; The distributions of pore pressure, vertical stress, shear stress and vertical displacement contours using the FEM and X-FEM meshes.

earthquake of 1971. Obviously, the results of X-FEM model are in good agreement with those obtained by the FEM analyzes. The above results clearly illustrate the performance of the X-FEM model in the failure analysis of the San Fernando dam.

5. Conclusion

In the present paper, an enriched finite element method was developed in modeling of deformable porous media. The extended finite element method was applied to the governing equations of porous media in an updated Lagrangian framework, followed by a generalized Newmark scheme used for the time domain discretization. The X-FEM was used in modeling of weak discontinuities, in which the process was accomplished by partitioning the domain with some triangular sub-elements whose Gauss points were used for integration of the domain of elements. Finally, three numerical examples of elastic soil column, elastic foundation, and the failure analysis of lower San–Fernando dam were modeled by the X-FEM technique to demonstrate the efficiency of the X-FEM technique in deformable porous soils, and the results were compared with those of standard FEM model. This research can be used in practical problems to present the parametric study and parametric design of deformable porous media, in which the material interfaces can easily be taken independent of the FE mesh to optimize various parameters of the model.
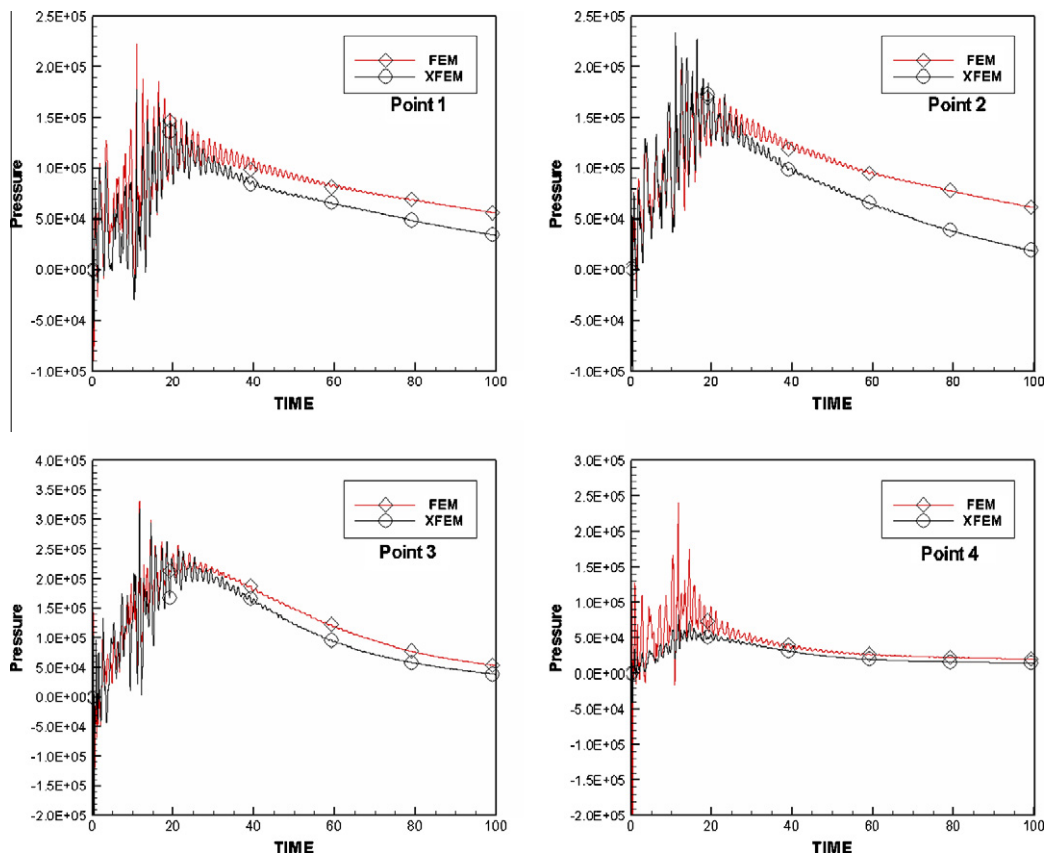
Fig. 11. The San–Fernando dam; the pressure history of FEM and X-FEM models at different nodes.

Appendix A

A.1. The modified Pastor–Zienkiewicz generalized plasticity model

The framework of Pastor–Zienkiewicz generalized plasticity model was first introduced by Pastor et al. [49] for fully saturated media and then developed by Zhang et al. [50] for partially saturated soils to model the behavior of soil under monotonic and cyclic loading. The main advantage of theory is that neither the yield surface nor plastic potential surface needs to be explicitly defined. In this model, the constitutive tensor in loading $\mathbf{C}_L$ differs from constitutive tensor in unloading $\mathbf{C}_U$, i.e. $d\boldsymbol{\varepsilon}_L = \mathbf{C}_L d\boldsymbol{\sigma}'$ and $d\boldsymbol{\varepsilon}_U = \mathbf{C}_U d\boldsymbol{\sigma}'$. In fact, at each point of the stress space, a direction tensor is specified to distinguish between loading and unloading. In generalized plasticity of Pastor–Zienkiewicz model, all necessary components of elasto-plastic constitutive matrix can be obtained without referring to the plastic potential, or yield surfaces.

In order to introduce the parameters of the model, a triaxial compression test may be applied. Considering $p' = J_1/3$, $q = \sqrt{3J_{2D}}$ and their work-associated strains invarients ε_v^p and ε_s^p, it can be shown that the dilatancy d_g can be approximated from the stress ratio $\eta = p'/q$ as

$$d_g = \frac{d\boldsymbol{\varepsilon}_v^p}{d\boldsymbol{\varepsilon}_s^p} = (1+\alpha)(M_g - \eta), \tag{A.1}$$

where α is a material parameter and M_g denotes the slope of critical state line. The normal vectors to the plastic potential and yield surfaces can be determined by

$$\mathbf{n}_g^T = (n_{gv}, n_{gs}) = (d_g, 1)\left/\sqrt{1+d_g^2}\right., \tag{A.2}$$

$$\mathbf{n}^T = (n_v, n_s) = (d_f, 1)\left/\sqrt{1+d_f^2}\right., \tag{A.3}$$

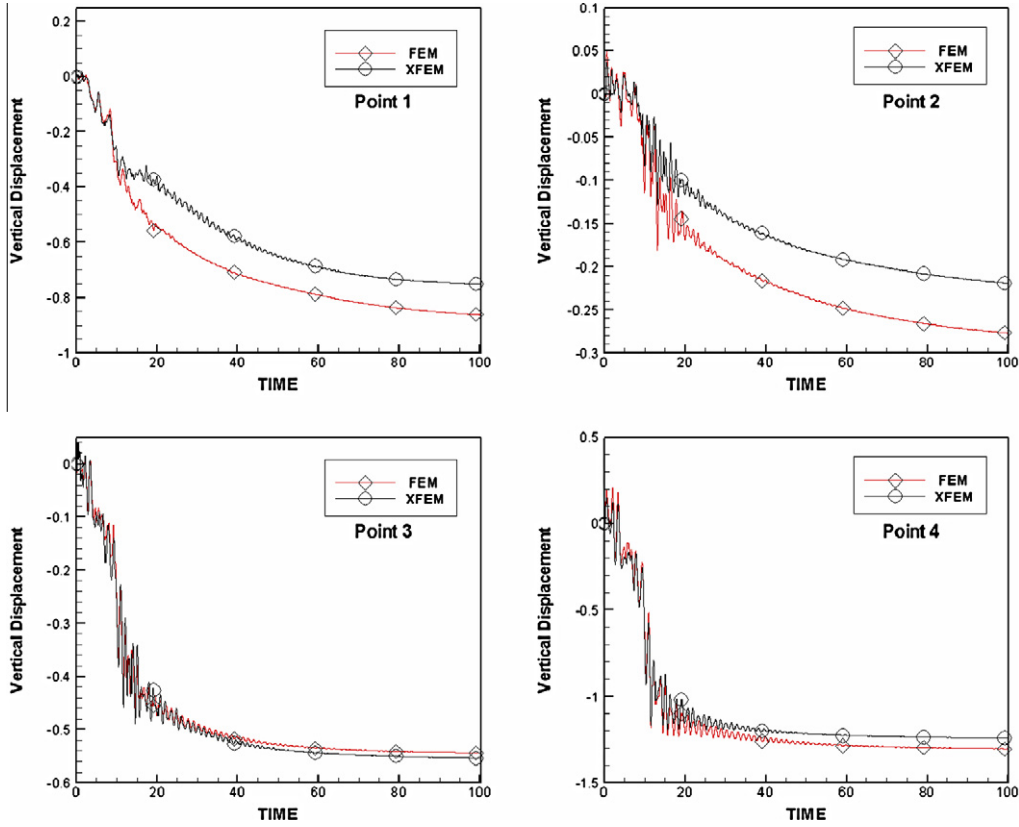where d_f is defined in a similar manner to d_g as

Fig. 12. The San–Fernando dam; the displacement history of FEM and X-FEM models at different nodes.
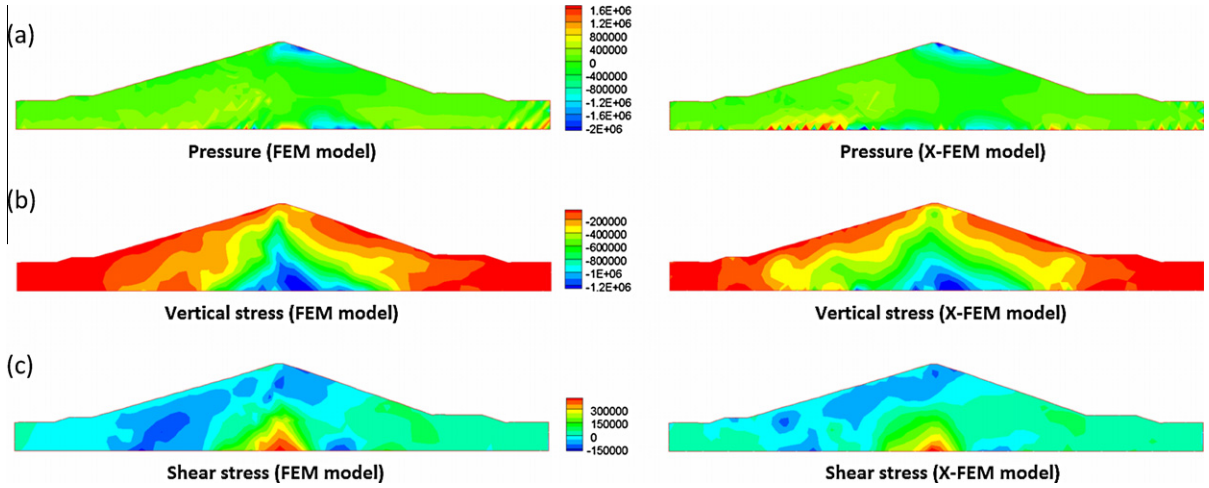

Fig. 13. Numerical results at 25 s after beginning of the earthquake for the lower San–Fernando dam; The distributions of pore pressure, vertical stress and shear stress contours using the FEM and X-FEM meshes.

$$d_f = (1 + \alpha)(M_f - \eta), \qquad (A.4)$$

where M_g/M_f is equal to relative density. In the case of $d_f = d_g$, the hardening rule is associated.

The plastic modulus H_L for the loading condition is defined by

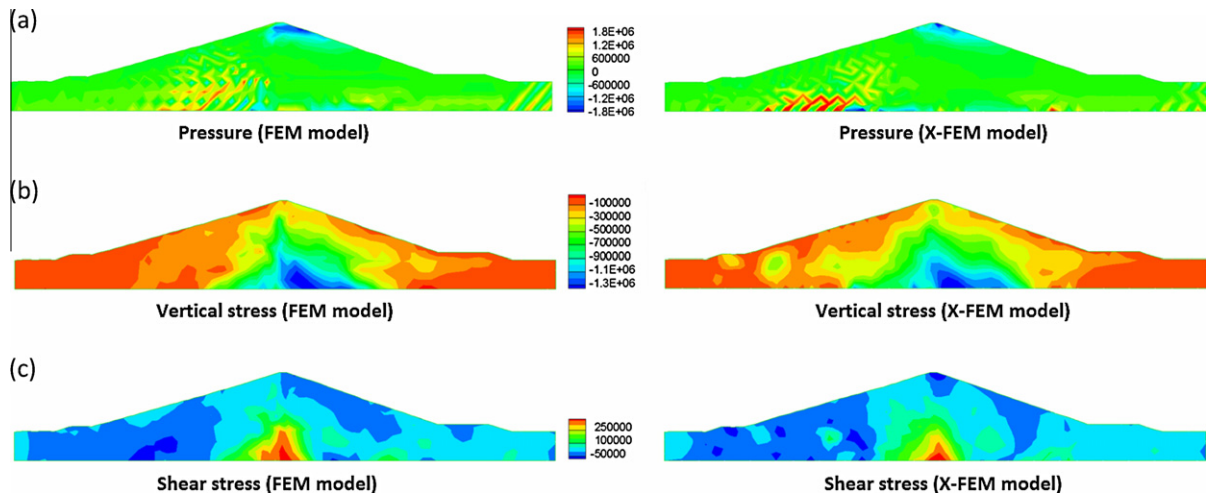$$H_L = H_0 p' H_f (H_v + H_s) H_{DM}, \qquad (A.5)$$

Fig. 14. Numerical results at 50 s after beginning of the earthquake for the lower San–Fernando dam; The distributions of pore pressure, vertical stress and shear stress contours using the FEM and X-FEM meshes.

where $H_f = (1 - \eta/\eta_f)^4$, $H_s = \beta_0\beta_1\exp(-\beta_0\xi)$, $H_v = (1 - \eta/M_g)$, $H_{DM} = (\zeta_{max}/\zeta)^\gamma$, $\eta_f = (1 + 1/\alpha)M_f$ and $\zeta = p'[1 - ((1 + \alpha)/\alpha)(\eta/M_g)]^{1/\alpha}$, with H_0, β_0, β_1 and γ_U denoting the material parameters obtained from experiments.

The plastic modulus H_U for unloading condition is defined by

$$H_U = H_{U0}(M_g/\eta_U)^{\gamma_U} \quad \text{for } |M_g/\eta_U| > 1,$$
$$H_{U0} \qquad\qquad \text{for } |M_g/\eta_U| \leqslant 1, \tag{A.6}$$

where H_{U0} is the material parameter and η_U is the stress ratio from which unloading takes place. The vector $\mathbf{n}_{gU}$ is defined as

$$\mathbf{n}_{gU} = (n_{gUv}, n_{gUs})^T = (-abs(n_{gv}), +n_{gs})^T. \tag{A.7}$$

In order to extend the model for partially saturated soil, the effective stress tensor and suction are assumed as independent stress variables. The effective stress is defined by $\sigma'_{ij} = \sigma_{ij} + \delta_{ij}(S_wp_w + S_gp_g)$, with p_w and p_g denoting the water and gas pressures, respectively, and the suction is defined by $s = p_c = p_g - p_w$. In modified Pastor–Zienkiewicz model, the plastic behavior of soil is assumed as a function of suction by modifying the hardening modulus, defined in equation (A.5), through the introduction of multiplicative function $\widetilde{H}_w$ that relates the variation of hardening to suction linearly. i.e.

$$H_L = H_0p'\widetilde{H}_wH_f(H_v + H_s)H_{DM}, \tag{A.8}$$

where $\widetilde{H}_w = 1 + as$, with a denoting a material parameter. In this model, the function $\widetilde{H}_w$ is determined as required to fit different experimental data. In some cases, a dependence of $\widetilde{H}_w$ on p' has to be assumed to describe the behavior of soil that exhibit a maximum collapse at some value of the mean stress. This feature can be dealt with above relation by assuming the dependence of a on the effective mean stress p' through the function $a = a_1\exp(-p') - a_2$. In this way, the original formulation of fully saturated soil can be recovered when suction is equal to zero.

References

[1] R. de Boer, Highlights in the historical development of the porous media theory: toward a consistent macroscopic theory, Appl. Mech. Rev. 69 (1996) 201–262.
[2] K. Terzaghi, Theoretical Soil Mechanics, Wiley, New York, 1943.
[3] M.A. Biot, General theory of three dimensional consolidation, J. Appl. Phys. 12 (1941) 155–164.
[4] M.A. Biot, Theory of propagation of elastic waves in a fluidsaturated porous solid, J. Acous. Soc. Am. 28 (1956) 168–191.
[5] M.A. Biot, Mechanics of deformation and acoustic propagation in porous media, J. Appl. Phys. 33 (1962) 1482–1498.
[6] L.W. Morland, A simple constitutive theory for simple saturated porous solids, Geophysics 77 (1972) 890–900.
[7] M.A. Goodman, S.C. Cowin, A continuum theory for granular materials, Arch. Rat. Mech. Anal. 44 (1979) 249–266.
[8] R. Sampaio, W.O. Williams, Thermodynamics of diffusing mixtures, de Mec. 18 (1979) 19–45.
[9] R.M. Bowen, Incompressible porous media models by use of the theory of mixtures, Int. J. Eng. Sci. 18 (1980) 1129–1148.
[10] R.M. Bowen, Compressible porous media models by use of theories of mixtures, Int. J. Eng. Sci. 20 (1982) 697–735.
[11] S. Whitaker, Simultaneous heat, mass and momentum transfer in porous media; a theory of drying, Adv. Heat Transfer 13 (1977) 119–203.
[12] M. Hassanizadeh, W.G. Gray, General conservation equations for multiphase systems. 1: averaging procedure, Adv. Water Resour. 2 (1979) 131–144.
[13] M. Hassanizadeh, W.G. Gray, General consevation equations for multiphase systems. 2: mass, momenta, energy and entropy equations, Adv. Water Resour. 2 (1979) 191–203.
[14] M. Hassanizadeh, W.G. Gray, General conservation equations for multiphase systems. 3: constitutive theory for porous media flow, Adv. Water Resour. 3 (1980) 25–40.
[15] D.G. Fredlund, N.R. Morgenstern, Stress state variables for unsaturated soils, J. Geotech. Eng. Div. ASCE 103 (1977) 447–466.

[16] C.S. Chang, J.M. Duncan, Consolidation analysis for partly saturated clay by using an elastic–plastic effective stress–strain model, Int. J. Numer. Anal. Methods Geomech. 7 (1983) 39–55.
[17] R. de Boer, S.J. Kowalski, A plasticity theory for fluid saturated porous media, Int. J. Eng. Sci. 21 (1983) 11–16.
[18] O.C. Zienkiewicz, A.H.C. Chan, M. Pastor, D.K. Paul, T. Shiomi, Static and dynamic behavior of soils; A rational approach to quantitative solution. I: fully saturated problems, Proc. R. Soc. London 429 (1990) 285–309.
[19] O.C. Zienkiewicz, Y.M. Xie, B.A. Schrefler, A. Ledesma, N. Bicanic, Static and dynamic behavior of soils; A rational approach to quantitative solution. II: semi-saturated problems, Proc. R. Soc. London 429 (1990) 311–321.
[20] E.E. Alonso, A. Gens, A. Josa, A constitutive model for partially saturated soils, Geotechnique 40 (1990) 405–430.
[21] B.A. Schrefler, X. Zhan, A fully coupled model for water flow and airflow in deformable porous media, Water Resour. Res. 29 (1993) 155–167.
[22] D. Gawin, P. Baggio, B.A. Schrefler, Coupled heat, water and gas flow in deformable porous media, Int. J. Numer. Methods Fluids 20 (1995) 969–987.
[23] D. Gawin, B.A. Schrefler, Thermo-hydro-mechanical analysis of partially saturated porous materials, Eng. Comput. 13 (1996) 113–143.
[24] J.M. Melenk, I. Babuska, The partition of unity finite element method: basic theory and applications, Comput. Methods Appl. Mech. Eng. 139 (1996) 289–314.
[25] J. Dolbow, An extended finite element method with discontinuous enrichment for applied mechanics, Ph.D. Thesis, Northwestern University, 1999.
[26] T. Belytschko, T. Black, Elastic crack growth in finite elements with minimal remeshing, Int. J. Numer. Methods Eng. 45 (1999) 601–620.
[27] N. Moës, J.E. Dolbow, T. Belytschko, A finite element method for crack growth without remeshing, Int. J. Numer. Methods Eng. 46 (1999) 131–150.
[28] C. Daux, N. Moës, J.E. Dolbow, N. Sukumar, T. Belytschko, Arbitrary branched and intersecting cracks with the extended finite element method, Int. J. Numer. Methods Eng. 48 (2000) 1741–1760.
[29] N. Sukumar, D.L. Chopp, N. Moës, T. Belytschko, Modeling holes and inclusions by level sets in the extended finite-element method, Comput. Methods Appl. Mech. Eng. 190 (2001) 6183–6200.
[30] T. Belytschko, N. Moës, S. Usui, C. Parimi, Arbitrary discontinuities in finite elements, Int. J. Numer. Methods Eng. 50 (2001) 993–1013.
[31] J.E. Dolbow, N. Moës, T. Belytschko, An extended finite element method for modeling crack growth with frictional contact, Comput. Methods Appl. Mech. Eng. 190 (2001) 6825–6846.
[32] N. Moës, T. Belytschko, Extended finite element method for cohesive crack growth, Eng. Fracture Mech. 69 (2002) 813–833.
[33] G. Ventura, E. Budyn, T. Belytschko, Vector level sets for description of propagating cracks in finite elements, Int. J. Numer. Methods Eng. 58 (2003) 1571–1592.
[34] P.M.A. Areias, T. Belytschko, Analysis of three-dimensional crack initiation and propagation using the extended finite element method, Int. J. Numer. Methods Eng. 63 (2005) 760–788.
[35] J. Réthoré, R. de Borst, M.A. Abellan, A two-scale approach for fluid flow in fractured porous media, Int. J. Numer. Methods Eng. 71 (2007) 780–800.
[36] S. Bordas, P.V. Nguyen, C. Dunant, A. Guidoum, H. Nguyen-Dang, An extended finite element library, Int. J. Numer. Methods Eng. 71 (2007) 703–732.
[37] B. Prabel, A. Combescure, A. Gravouil, S. Marie, Level set X-FEM non-matching meshes: application to dynamic crack propagation in elasto-plastic media, Int. J. Numer. Methods Eng. 69 (2006) 1553–1569.
[38] T. Elguedj, A. Gravouil, A. Combescure, Appropriate extended functions for X-FEM simulation of plastic fracture mechanics, Comput. Methods Appl. Mech. Eng. 195 (2006) 501–515.
[39] A.R. Khoei, M. Nikbakht, An enriched finite element algorithm for numerical computation of contact friction problems, Int. J. Mech. Sci. 49 (2007) 183–199.
[40] T.Y. Kim, J. Dolbow, T. Laursen, A mortared finite element method for frictional contact on arbitrary interfaces, Comput. Mech. 39 (2007) 223–236.
[41] A.R. Khoei, S.O.R. Biabanaki, M. Anahid, Extended finite element method for three-dimensional large plasticity deformations, Comput. Methods Appl. Mech. Eng. 197 (2008) 1100–1114.
[42] M. Anahid, A.R. Khoei, New development in extended finite element modeling of large elasto-plastic deformations, Int. J. Numer. Methods Eng. 75 (2008) 1133–1171.
[43] A.R. Khoei, M. Anahid, K. Shahim, An extended arbitrary Lagrangian–Eulerian finite element method for large deformation of solid mechanics, Finite Elem. Anal Des. 44 (2008) 401–416.
[44] M. Anahid, A.R. Khoei, Modeling of moving boundaries in large plasticity deformations via an enriched arbitrary Lagrangian–Eulerian FE method, Scientia Iranica, J. Civil Eng. 17 (2010) 141–160.
[45] A.R. Khoei, K. Karimi, An enriched-FEM model for simulation of localization phenomenon in Cosserat continuum theory, Comput. Mat. Sci. 44 (2008) 733–749.
[46] A.R. Khoei, A.R. Azami, S.M. Haeri, Implementation of plasticity based models in dynamic analysis of earth and rockfill dams; A comparison of Pastor–Zienkiewicz and cap models, Comput. Geotech. 31 (2004) 385–410.
[47] A.R. Khoei, R.W. Lewis, O.C. Zienkiewicz, Application of the finite element method for localized failure analysis in dynamic loading, Finite Elem. Anal. Des. 27 (1997) 121–131.
[48] A.R. Khoei, S.A. Gharehbaghi, A.R. Tabarraie, A. Riahi, Error estimation, adaptivity and data transfer in enriched plasticity continua to analysis of shear band localization, Appl. Math. Model. 31 (2007) 983–1000.
[49] M. Pastor, O.C. Zienkiewicz, A.H.C. Chan, Generalized plasticity and the modeling of soil behavior, Int. J. Numer. Anal. Methods Geomech. 14 (1990) 151–190.
[50] H.W. Zhang, O.M. Heeres, R. de Borst, B.A. Schrefler, Implicit integration of a generalized plasticity constitutive model for partially saturated soil, Eng. Comput. 18 (2001) 314–336.
[51] A.R. Khoei, S.A. Gharehbaghi, A.R. Azami, A.R. Tabarraie, SUT–DAM: an integrated software environment for multi-disciplinary geotechnical engineering, Adv. Eng. Softw. 37 (2006) 728–753.
[52] A.R. Khoei, T. Mohamadnejad, Numerical modeling of multiphase fluid flow in deforming porous media; A comparison between two- and three-phase models for seismic analysis of earth and rockfill dams, Comput. Geotech. 38 (2011) 142–166.